Title

Evaluation of the 3D caesponse of geosynthetic reinforced soil bridge abutments under service load conditions

Journal

Geotextiles and Geomembranes, 54(5)

ISSN

0266-1144

Authors

Deng, Jialong
Guo, Wenhao
Fox, Patrick J
et al.

Publication Date

2026-10-01

DOI

10.1016/j.geotexmem.2026.05.003

Evaluation of the 3D response of geosynthetic reinforced soil bridge abutments under service load conditions

Jialong Deng[a], Wenhao Guo[b], Patrick J. Fox[c], John S. McCartney[d], Yewei Zheng[e,*]

[a] *Ph.D. Candidate, School of Civil Engineering, Wuhan University, Wuhan, Hubei 430072, China; Email: tangkalung@whu.edu.cn; ORCID Number: 0000-0001-8343-5736*

[b] *Intermediate Engineer, Power China Zhongnan Engineering Corporation Limited, Changsha, Hunan, 410014, China; formerly Ph.D. Student, School of Civil Engineering, Wuhan University, Wuhan, Hubei 430072, China; Email: guowenhao@whu.edu.cn; ORCID Number: 0000-0003-4695-3934*

[c] *Professor and Dean, Russ College of Engineering and Technology, Ohio University, Athens, OH 45701 USA; Email: pfox@ohio.edu; ORCID: 0000-0003-2109-0378*

[d] *Professor, Department of Structural Engineering, University of California, San Diego, La Jolla, CA 92093-0085 USA; Email: mccartney@ucsd.edu; ORCID: 0000-0001-7279-3490*

[e] *Professor, School of Civil Engineering, Wuhan University, Wuhan, Hubei 430072 China; Email: yzheng@whu.edu.cn (*corresponding author); ORCID: 0000-0001-9038-4113*

Abstract: This paper presents 3D numerical simulations of GRS bridge abutments under different conditions of bridge surcharge stress, with the goal of better understanding 3D deformation behavior and evaluating the internal stability for 3D loading conditions. Backfill soil was modeled using a nonlinear elastoplastic model with the Duncan–Chang hyperbolic stress–strain relationship and the Mohr–Coulomb failure criterion. A corresponding 2D model representative of that typically used in the routine analysis and design of GRS bridge abutments was also developed for comparison. Results show that the facing displacements, bridge seat settlements, and maximum reinforcement tensile forces obtained from the 2D simulations are close to those of the longitudinal centerline section in the 3D simulations. These findings suggest that 2D simulations can reasonably predict the deformations and reinforcement tensile requirements in bridge abutments despite the simplified plane strain assumption. Parametric analyses further reveal that facing displacements increase with abutment width but stabilize for larger widths, while abutment width has a negligible influence on bridge seat settlements. Increasing abutment height results in greater facing displacements, bridge seat settlements, and reinforcement tensile forces due to increased stress levels within the abutment structure.

Keywords: Geosynthetic; Geosynthetic reinforced soil; Bridge abutment; Numerical simulation; Reinforcement tensile force

1. Introduction

In recent years, geosynthetic reinforced soil (GRS) structures have been increasingly used as bridge abutments to support bridge superstructures. Several case histories of in-service GRS bridge abutments have been reported and indicated good service performance, especially in reducing differential settlements between the bridge and approach embankments (Abu-Hejleh et al. 2002; Saghebfar et al. 2017; Talebi et al. 2017; Adams and Nicks 2018; Gebremariam et al. 2020a, 2020b; Zhang et al. 2022).

In field monitoring programs, the performance of GRS bridge abutments is typically evaluated using measured data along vertical cross sections in the longitudinal direction, while facing displacements and reinforcement tensile forces in the transverse direction are neglected. Although multiple sections were monitored in some projects, all were oriented in the longitudinal direction (Saghebfar et al. 2017; Gebremariam et al. 2020a, 2020b; Zhang et al. 2022). Similarly, most of the laboratory model tests in previous studies for GRS bridge abutments were designed under the 2D plane strain conditions (Wu et al. 2001, 2006; Pham 2009; Nicks et al. 2013, 2016; Adams et al. 2014; Iwamoto et al. 2015; Xiao et al. 2016; Xu et al. 2019; Deng et al. 2023; Verma and Mittal, 2023; Jia et al. 2025; Wang et al. 2025), and the behavior in the transverse section has rarely been considered.

Field monitoring programs and laboratory model tests have made significant contributions to the understanding of the behavior of GRS bridge abutments under service load conditions; however, these tests are costly and time-consuming. Thus, numerical modeling is often used as an effective tool to complement experimental research results. Two-dimensional (2D) plane strain conditions have been typically assumed in numerical simulations of GRS bridge abutments (Helwany et al. 2003, 2007; Skinner and Rowe 2005; Xie and Leshchinsky 2015; Ambauen et al. 2016; Zheng and Fox 2016, 2017; Zheng et al. 2018; Ardah et al. 2017, 2021; Shen et al. 2020; Gebremariam et al. 2021; Deng et al. 2025; Jia et al. 2025). Simulation results from these 2D numerical studies generally indicate that the reinforcement spacing and stiffness, soil friction angle, and bridge load are the primary factors influencing the deformations of GRS bridge abutments. Zheng et al. (2017) compared the maximum tensile forces from 2D simulations with the calculated values using the methods in the current design guidelines based on the plane strain conditions. Comparisons show that both the FHWA method (Adams and Nicks 2018) and the AASHTO method (AASHTO 2020) overestimate the maximum tensile forces, with the FHWA method being more conservative. These discrepancies highlight the need for 3D simulations to better capture the critical behavior conditions of GRS bridge abutments beyond the traditional 2D analyses.

Despite the important insights from the 2D simulations, comparisons between the 2D and 3D numerical simulations of GRS bridge abutments have been made to assess the accuracy of the 2D model and investigate the discrepancies between the 2D and 3D behavior (Abu-Farsakh et al. 2018; Zheng et al. 2022). Abu-Farsakh et al. (2018) and Zheng et al. (2022) found that deformations from the 3D simulations were slightly smaller than those from the 2D simulations, which are generally in reasonable agreement with the measurements from field instrumentation (Abu-Farsakh et al. 2018) and half-scale model test (Zheng et al. 2022), respectively. Similar observations were also reported by Shen et al. (2019) based on the 2D and 3D numerical simulations of GRS mini-piers. These findings generally indicate that 2D simulations tend to be slightly more conservative in terms of deformations and can provide reasonable estimations; however, the 2D models cannot provide information for sections other than the longitudinal section.

GRS bridge abutments are 3D structures with one front wall and two side walls, and thus additional information is needed regarding facing displacements and tensile forces in different sections for a comprehensive evaluation. However, research on the 3D behavior of GRS bridge abutments remain limited (Rong et al. 2017; Abu-Farsakh et al. 2018; Zheng et al. 2019). Rong et al. (2017) conducted a 3D numerical study of a full-scale GRS bridge abutment. The simulation results indicate that placement of the superstructure induces deformations of GRS bridge abutment in the longitudinal and transverse directions, and the facing displacements of the side wall are smaller than those of the front wall, which is consistent with experimental data from half-scale model tests reported by Zheng et al. (2019a). Apart from the limited research on the deformation behavior, the effect of 3D boundary conditions, such as the abutment width and height, on the reinforcement tensile strain distribution and maximum tensile forces, especially for the transverse reinforcement layers, has not been investigated. Therefore, a comprehensive investigation is needed to understand the internal stability of GRS bridge abutments for 3D conditions and evaluate the accuracy of current design methodologies.

This paper presents 3D numerical simulations of the static response of GRS bridge abutments to better illustrate the 3D deformation behavior and internal stability for 3D conditions. A 2D numerical simulation is also presented to compare the differences between the 2D and 3D response and to assess the accuracy of the plane strain assumption in the current analysis methods. Furthermore, a parametric study is conducted to investigate the influences of abutment width and abutment height on the 3D response of GRS bridge abutments. Results provide valuable insights into the deformation behavior and internal stability design of GRS bridge abutments.

2. Numerical model

In this study, the finite difference program FLAC3D Version 5.0 (Itasca 2015) was used for the numerical simulations of GRS bridge abutments. A FLAC3D model was developed by Zheng et al. (2022) to simulate the 3D response of a half-scale GRS bridge abutment specimen. Comparisons between the simulated and measured results are in good agreement, which indicates that the 3D numerical model could accurately capture the static response of GRS bridge abutments. Therefore, the validated numerical model is used in this study to investigate the 3D static response of full-scale GRS bridge abutments. In addition, a 2D simulation of the mid-abutment section of the abutment was performed using plane strain conditions, which is typically assumed in routine analysis and design of GRS walls in general, is conducted to illustrate discrepancies between the 2D and 3D responses of full-scale GRS bridge abutments.

2.1 Model geometry and configuration

Model geometry and configuration of the GRS bridge abutment system are shown in Figure 1. Half of the bridge system, including one GRS bridge abutment, was simulated considering symmetry of geometry. The 3D numerical model includes a foundation soil layer, an embankment, a GRS bridge abutment, a bridge seat, and a bridge beam. This model configuration is different from the geosynthetic reinforced soil-integrated bridge system (GRS-IBS) developed by the FHWA (Adams and Nicks 2018), in which the bridge beam is placed on a beam seat composed of geosynthetic wrapped reinforced soil layer. However, this model with the beam placed on a concrete bridge seat with backwall follows recommendations with seismic concerns from the California Department of Transportation (Caltrans). The bottom boundary of the foundation layer was fixed in the x, y, and z directions. All four lateral boundaries of the model were fixed in the direction perpendicular to the boundary and free to move parallel to the boundary.

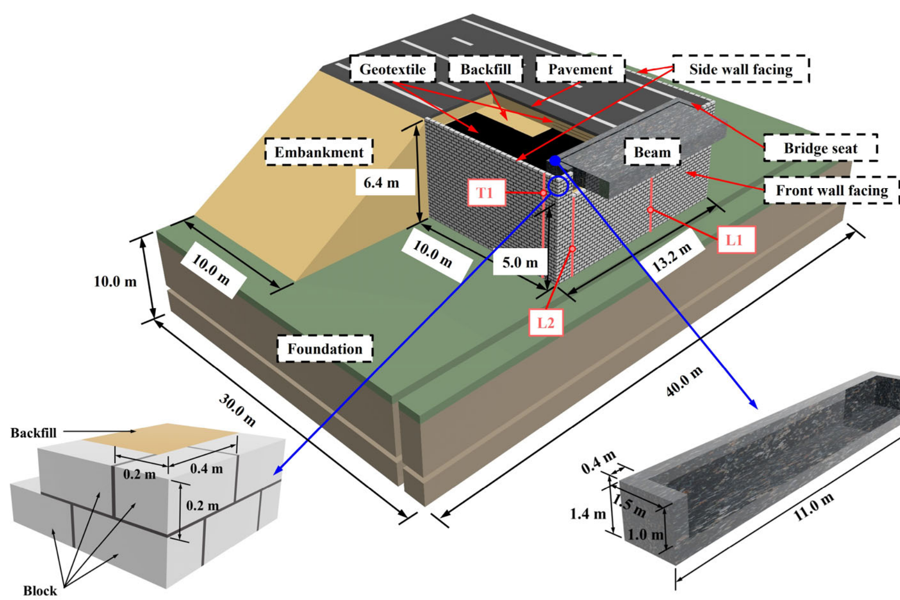

(a)

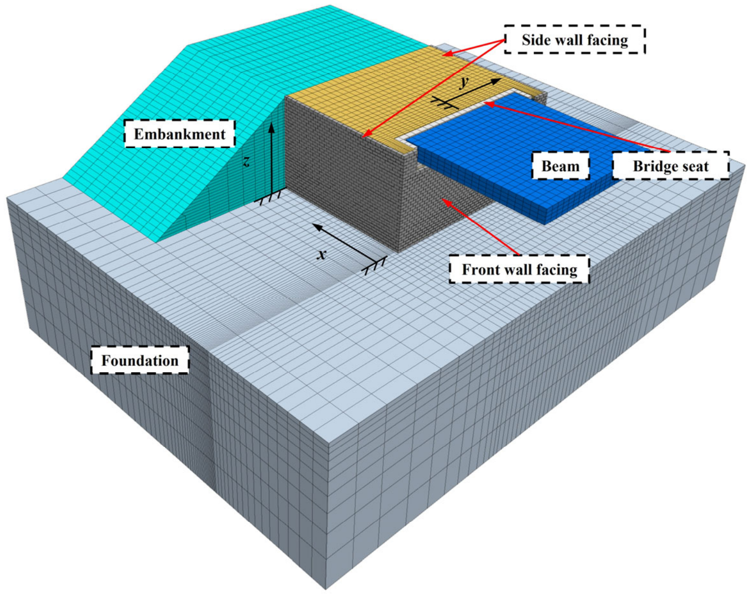

(b)

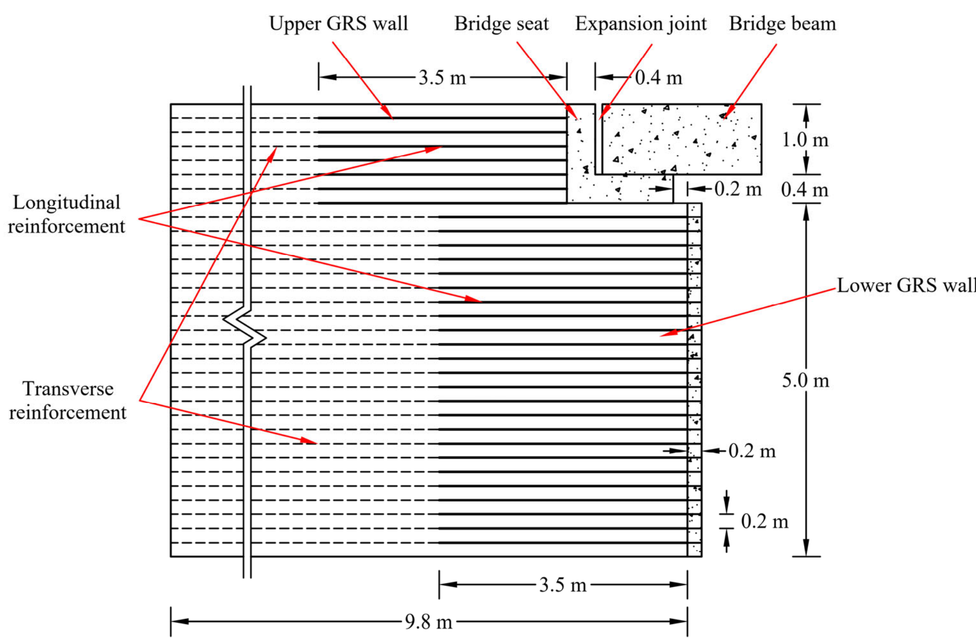

(c)

Figure 1 3D numerical model for GRS bridge abutment: (a) model configuration; (b) finite difference grid; (c) longitudinal cross-section

The foundation soil layer has plan dimensions of 30 m × 40 m and depth of 10 m. A 6.4 m-high embankment with 1:1.5 side slope supports the back of GRS bridge abutment. The vertical side of the embankment that supports the abutment was fixed in the *x* direction prior to construction, and the area in contact with the backfill soil was set free with increasing elevation as the construction proceeded. The GRS bridge abutment has a width of 13.2 m in the *y* direction and a length of 10.0 m in the *x* direction. The GRS bridge abutment has a total height of H = 6.4 m, consisting of a 5-m-high lower GRS wall (h = 5 m) under the bridge seat and a 1.4-m-high upper GRS wall behind the bridge seat. Both the lower and upper GRS walls are composed of 0.2-m-thick alternating layers of well compacted backfill soil and closely spaced geotextile reinforcement. A 0.2-m-thick concrete pavement layer was placed on the top of the upper GRS wall. The GRS bridge abutment has modular block facing for the front wall and two side walls. The concrete modular blocks have dimensions of 0.4 m × 0.2 m × 0.2 m (length × width × height), as shown in Figure 1(a).

The simply-supported bridge beam with a total length of L_b = 20 m (half-length of 10 m as shown in Figure 1a) and a width of W = 10 m rests on the GRS bridge abutment through the bridge seat. The bridge seat has plan dimensions of 11.0 × 1.5 m and thickness of 0.4 m. The width of the expansion joint between the bridge beam and bridge seat on three sides is 0.1 m. The setback distance between the bridge seat and back of front wall is 0.2 m, and the distance between the bridge seat and side walls is 0.9 m.

A corresponding 2D numerical model of the longitudinal slice with a thickness of 0.4 m (equivalent to the length of one facing block) in the *y*-direction was also developed using FLAC3D. The same modeling approach of the 3D simulation, including constitutive models and parameters, was applied to the 2D model to enable direct comparison

2.2 Soils

The backfill soil is a well graded sand with maximum particle size of 9.5 mm and peak friction angle of 46°, as reported by Zheng et al. (2018b), which meets the requirements for GRS bridge abutments (Berg et al. 2009; Adams and Nicks 2018). Backfill soils with similar friction angles have been reported in several case histories (Gebrenegus et al. 2015; Adams and Nicks 2018). The backfill soil was modeled as a nonlinear elastic-plastic material with the Duncan–Chang hyperbolic stress–strain relationship (Duncan et al. 1980) and the Mohr–Coulomb failure criterion. This constitutive model accounts for the nonlinear behavior of soil and has been successfully used to simulate the static behavior of GRS bridge abutments under service load conditions (Zheng and Fox 2016, 2017). Details of the model have been reported by Zheng et al. (2022).

The backfill soil parameters were calibrated according to the results of consolidated drained triaxial compression tests for sand specimens compacted at a relative density of 80%, as reported by Zheng et al. (2018b). Figure 2 shows the comparison between the results from the tests and simulations. The simulated nonlinear stress-strain behavior prior to peak strength is in good agreement with the measurements for different stress levels. The post-peak strain softening response and the dilation behavior at high levels of axial strain are not captured by the model. However, these are not expected to significantly affect the findings of the current study that focuses on service load conditions (Zheng et al. 2018b).

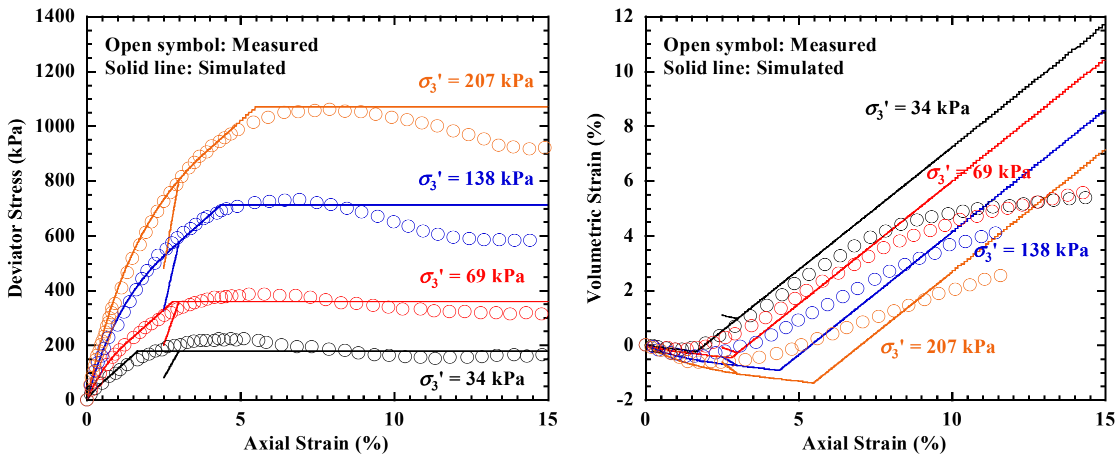

(a) (b)

Figure 2 Comparison of measured and simulated triaxial test results along with a simulated unloading path: (a) deviator stress; (b) volumetric strain

The foundation soil and embankment soil were specified as a dense granular soil and modeled using a linearly elastic–perfectly plastic model with the Mohr–Coulomb failure criterion. Model parameters for the backfill soil, foundation soil, and embankment soil are listed in Table 1. An apparent cohesion of 1 kPa for the backfill soil and 2 kPa for the embankment soil was used to account for the effects of unsaturated conditions.

Table 1 Soil parameters

Property	Value
Backfill soil	
Total unit weight, γ (kN/m^3)	17.3
Elastic modulus number, K	334
Unloading–reloading elastic modulus number, K_{ur}	401
Elastic modulus exponent, n	0.66
Failure ratio, R_f	0.67
Bulk modulus number, B	254
Bulk modulus exponent, m	0
Atmospheric pressure, P_a (kPa)	101.3
Apparent cohesion, c' (kPa)	1.0
Friction angle, ϕ' (degree)	46

Dilation angle, ψ (degree)	18
Foundation and embankment soil	
Total unit weight, γ (kN/m^3)	20.0
Elastic modulus, E (MPa)	80
Poisson's ratio, ν	0.3
Apparent cohesion, c' (kPa)	2.0
Friction angle, ϕ' (degree)	42
Dilation angle, ψ (degree)	12

2.3 Reinforcement

The geosynthetic reinforcement is a woven geotextile commonly used in GRS bridge abutments (Adams and Nicks 2018). The reinforcement vertical spacing is S_v = 0.2 m for both the lower and upper GRS walls. In each soil lift, three pieces of geotextile layer were placed in the lower GRS wall for the front wall and two side walls, respectively, as shown in Figure 1(a). The reinforcement layers have a uniform length of L_r = 3.5 m (0.7h) in the direction perpendicular to the wall facing for all three sides. For the upper GRS wall, the reinforcement length is also L_r = 3.5 m behind the bridge seat and two side walls. The geotextile layers were stacked between the blocks, forming frictional connections between the reinforcements and facing blocks. The geotextile was modeled using linearly elastic geogrid elements with isotropic behavior and tensile stiffness J = 1000 kN/m. According to Zheng et al. (2018), the linear reinforcement model is sufficiently accurate for the static response of GRS bridge abutments under service load conditions. The Poisson's ratio of the geotextile was selected as ν = 0.1 to simulate the out-of-plane behavior of woven geotextile (Soderman and Giroud 1995).

2.4 Structural components

The modular facing blocks, bridge seat, bridge beam, and pavement were modeled as linear elastic concrete materials with elastic modulus of E = 20 GPa, and Poisson's ratio of ν =

0.2. The concrete facing blocks, bridge seat, and pavement had a total unit weight of γ = 24 kN/m^3, whereas the unit weight for the bridge beam was adjusted based on the desired average vertical stress applied to the top of the lower GRS wall.

2.5 Interfaces

Various interfaces were implemented in the numerical models to simulate the interaction between different components of the GRS bridge abutment system, as shown in Figure 3. The block-block interface, geotextile-block interface, soil-geotextile interface, and soil-block interface are shown in Figure 3(a). Figure 3(b) shows the bridge seat-beam interface and the bridge seat-soil interface. The vertical bridge seat-beam interface on three sides were not in contact initially (i.e., 10 cm-wide expansion joints) but were included to account for possible contact due to deformations.

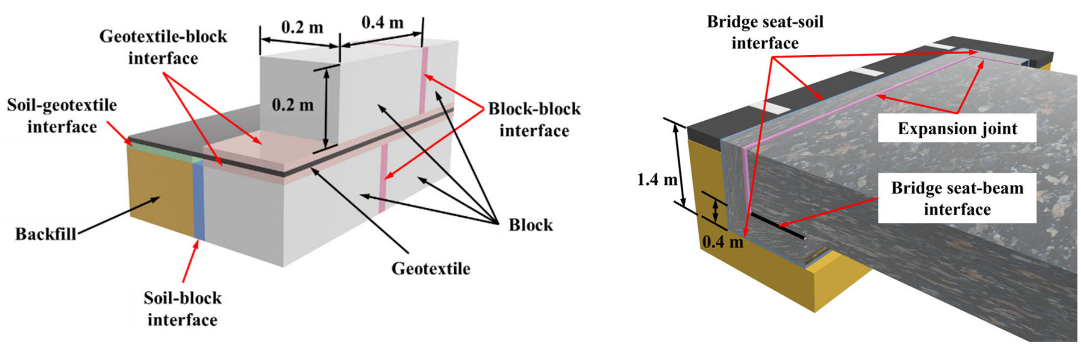

(a) (b)

Figure 3 Interface details: (a) GRS wall and facing; (b) bridge seat and bridge beam

Interface shear strength parameters were defined by interface friction angle δ_i' and adhesion c_i'. For soil interfaces, shear strength parameters were obtained by applying a strength reduction factor RF_i to the shear strength parameters of soil, where RF_i is defined as,

$$RF_i = \frac{\tan \delta_i'}{\tan \phi_s'} = \frac{c_i'}{c_s'} \tag{1}$$

The shear strength parameters for soil interfaces are provided in Table 2. For the block-block interface, geotextile-block interface, and bridge seat-beam interface, shear strength parameters were selected according to data from previous studies. The values of normal stiffness k_n and shear stiffness k_s of interfaces were determined according to the FLAC Manual (Itasca Consulting Group 2015).

Table 2 Interface parameters

Soil–Geotextile [a]	
Friction angle, δ_i' (°)	41.4
Adhesion, c_i' (kN/m/m)	0
Normal stiffness, k_n (GPa/m)	/
Shear stiffness, k_s (MPa/m)	4
Soil–Block and Soil–Seat [b]	
Friction angle, δ_i' (°)	33.9
Adhesion, c_i' (kPa)	0
Normal stiffness, k_n (GPa/m)	100
Shear stiffness, k_s (MPa/m)	400
Block–Block [c]	
Friction angle, δ_i' (°)	36.0
Adhesion, c_i' (kPa)	0
Normal stiffness, k_n (GPa/m)	100
Shear stiffness, k_s (MPa/m)	400
Block–Geotextile [d]	
Friction angle, δ_i' (°)	35.0
Adhesion, c_i' (kPa)	0
Normal stiffness, k_n (GPa/m)	/
Shear stiffness, k_s (MPa/m)	400
Bridge seat–Beam [e]	
Friction angle, δ_i' (°)	21.8
Adhesion, c_i' (kPa)	0
Normal stiffness, k_n (GPa/m)	100
Shear stiffness, k_s (MPa/m)	400

[a] Based on average of data (RF_i = 0.85) from Vieira et al. (2013).
[b] Based on data (RF_i = 0.65) from Ling et al. (2010).

[c] Based on data reported by Yu et al. (2016).
[d] Based on data reported by the Unified Facilities Guide Specifications (UFGS 2008).
[e] Based on coefficient of friction of 0.4 for elastomeric bearing pad suggested by the California Department of Transportation (Caltrans 1994).

2.6 Modeling procedures

The FLAC numerical model, including the foundation soil, embankment, GRS bridge abutment, and bridge beam, was numerically constructed in stages to better simulate the actual construction process. The lower GRS wall was constructed in 25 layers with each layer consisting of one 0.2-m-thick soil lift, one layer of blocks with three sides, three pieces of geotextile layer, and interfaces between different components. During construction of each layer, the corresponding gridpoints of embankment support in contact with the compacted backfill soil were unrestrained. Meanwhile, a temporary uniform vertical surcharge stress of 8 kPa was applied on the top surface of soil lift, and then removed prior to placement of the next lift for simulating the compaction effects (Hatami and Bathurst 2006; Zheng et al. 2018, 2022). The bridge seat was placed on the top of the lower GRS wall, and the upper GRS wall was constructed in the same manner behind the bridge seat. The pavement layer was then placed on the upper GRS wall. Finally, the bridge beam with a constant length of 10 m for the half-model (representing a total beam length of 20 m for the entire bridge) and an initial unit weight of γ = 8.4 kN/m^3 was placed on the bridge seat to produce an average vertical stress of q_v = 50 kPa on the lower GRS wall. Higher vertical stresses of q_v = 100 kPa, 200 kPa, 300 kPa, and 400 kPa were applied in stages by increasing the unit weight of bridge beam with a constant length of 10 m. Current FHWA design guidelines (Adams and Nicks 2018) recommend a maximum allowable vertical stress of 200 kPa for the service load conditions. The static response of GRS bridge abutments under the high vertical stresses of q_v = 300 kPa and 400 kPa is investigated, as the good service performance of GRS bridge abutments might allow for increasing the service limit (i.e., q_v = 200 kPa) for higher stresses (Nicks et al. 2016).

3. Simulation results

Simulation results are presented for three sections of the 3D model, including the longitudinal centerline section L1, the longitudinal section L2 (5.5 m away from the longitudinal centerline section under the edge of bridge seat), and the transverse section T1 (under the transverse centerline of bridge seat), and the 2D longitudinal model, as indicated in Figure 1(a). The results include wall facing displacements, bridge seat settlements, and reinforcement tensile strains and forces, under values of applied vertical stress q_v ranging from 50 kPa to 400 kPa.

3.1 Facing displacements

Figure 4(a) presents the facing displacement profiles for different sections under the service limit stress of 200 kPa. Facing displacement profiles for the 3D simulations have similar shapes with the maximum values located at approximately 2/3 of the wall height for the longitudinal sections and at mid-height for the transverse section. Facing displacements for the longitudinal centerline section L1 are larger than those for longitudinal section L2, both of which are greater than for transverse section T1. These results indicate that the application of bridge load produced outward wall deformations in both longitudinal and transverse directions, and thus indicating 3D deformation behavior of the abutment. For the 2D simulation, facing displacements for the front wall are larger than those for the longitudinal sections of the 3D simulation. This is mainly attributed to the differences in boundary conditions. In the 3D simulation, facing displacements are permitted for the front wall and two side walls, but only for the front wall in the 2D simulation. In addition, the shear stresses developed between the adjacent longitudinal sections may reduce the facing displacements to some extent in the 3D simulation, while frictionless side boundaries (i.e., plane strain) were specified for the 2D simulation.

Figure 4(b) shows the maximum facing displacements for different sections and values of applied vertical stress q_v ranging from 0 to 400 kPa. Maximum displacements for longitudinal sections L1 and L2 first increase linearly with increasing vertical stress up to 100 kPa and then increase at a higher rate with L1 having larger displacements than L2, while the transverse section T1 shows a linear trend with smaller displacements for the indicated range of vertical stress. Maximum displacements for the 2D simulation show a similar trend to those of L1 for the 3D simulation with a consistently larger displacement of approximately 2 mm. These results indicate that the 2D simulation is more conservative with regard to facing displacements than the 3D simulation.

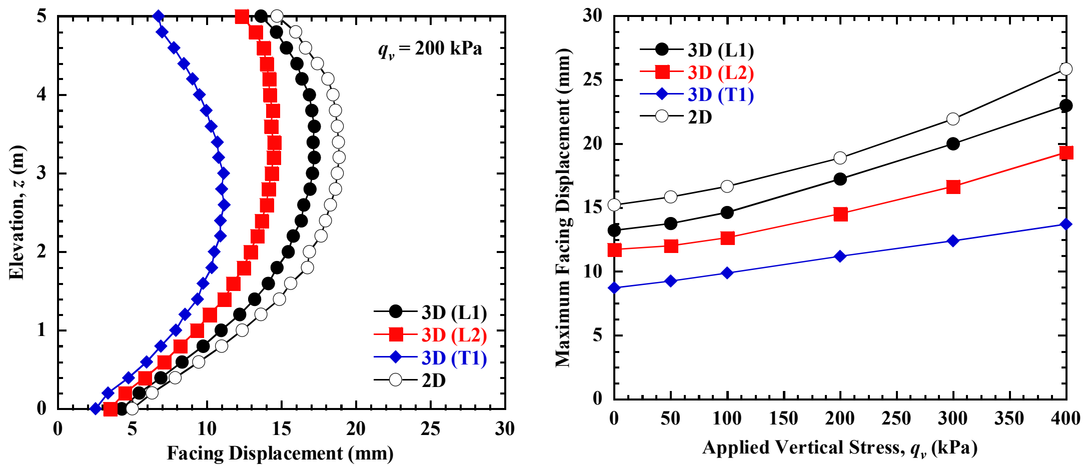

(a) (b)

Figure 4 Facing displacements: (a) vertical profiles under q_v = 200 kPa; (b) maximum displacements

Figure 5 presents horizontal profiles of facing displacements for the front and side walls of the 3D numerical model at elevation z = 3.0 m under different levels of vertical stress. In Figure 5(a), facing displacements of the front wall for the 3D model at different vertical stress levels are similar, with the minimum values at the edge of front wall and the maximum values at the center. As the vertical stress increases from 50 kPa to 400 kPa, the minimum facing displacement at the edge increases from 9.4 mm to 13.3 mm, and the maximum displacement at the center increases from 14.2 mm to 22.5 mm. The discrepancy of displacements between the edge and the center under the same applied vertical stress also increases from 4.8 mm to 9.2 mm, which indicates that the 3D deformation response is more pronounced for a higher bridge surcharge stress.

Figure 5(b) shows that the applied vertical stress has an important influence on facing displacements for the side wall under the bridge seat (i.e., x = 0.4 m – 1.9 m), and the influencing distance is approximately 6 m from the front wall facing. The maximum facing displacement is 10.9 mm at x = 4.4 m for q_v = 50 kPa and increases to 13.8 mm at x = 2.0 m for q_v = 400 kPa due to the increased vertical load on the bridge seat.

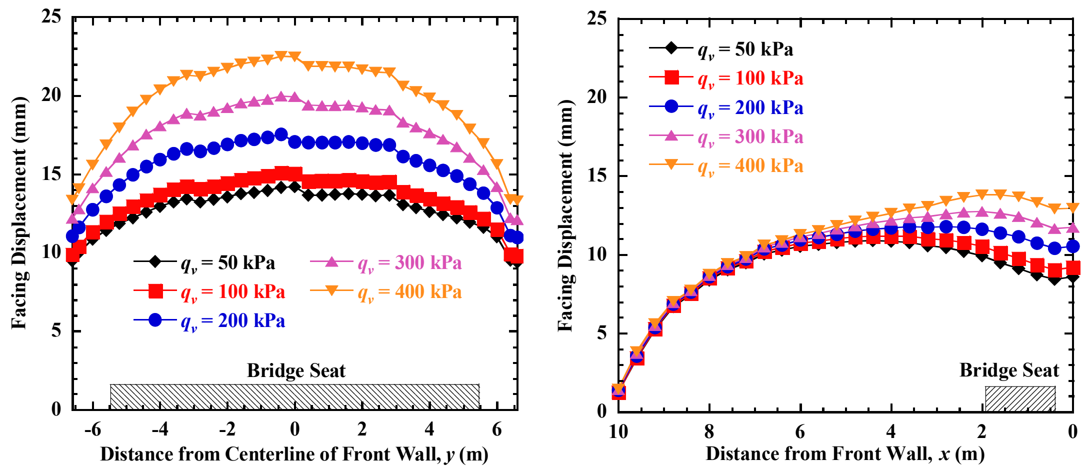

(a) (b)

Figure 5 Horizontal profiles of facing displacements at elevation z = 3.0 m: (a) front wall; (b) side wall

3.2 Bridge seat settlements

Figure 6 shows average bridge seat settlements given by the 2D and 3D simulations, which are calculated as the average value of the bridge seat settlements at x = 0.4 m and x = 1.9 m. Results show that the simulated average settlements of the longitudinal sections L1 and L2 are the same because the concrete bridge seat is rigid. Average settlements for the 2D simulations are essentially the same as those for the 3D simulations for vertical stress $q_v \leqslant$ 200 kPa but slightly larger than the 3D simulations for higher vertical stresses. In general, bridge seat settlements from the 2D and 3D simulations are in close agreement for the range of applied stresses investigated.

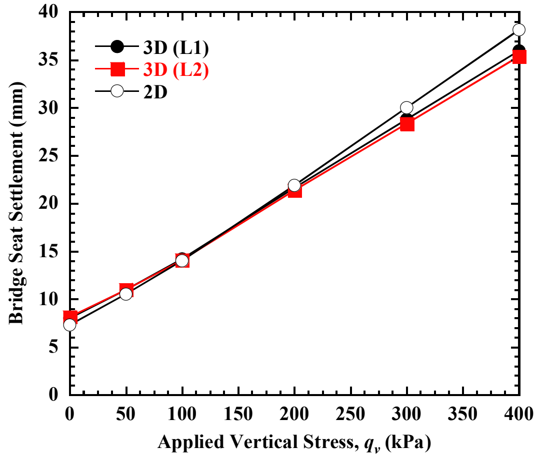

Figure 6 Bridge seat settlements

3.3 Reinforcement tensile strains

Figure 7 presents distributions of tensile strains for geosynthetic reinforcement layers under vertical stress q_v = 200 kPa. The profiles of tensile strain for the longitudinal sections L1 and L2 have similar shapes, with the maximum strain occurring near the facing connection and then decreasing toward the free end of the layer. The tensile strains for section L1 are slightly larger than those for section L2 for all reinforcement layers, especially under the bridge seat. The tensile strains obtained from the 2D simulation are slightly larger than those for section L1. In general, tensile strains from the 2D simulation are slightly more conservative than from 3D simulation, which is consistent with the results for displacement of the front wall facing.

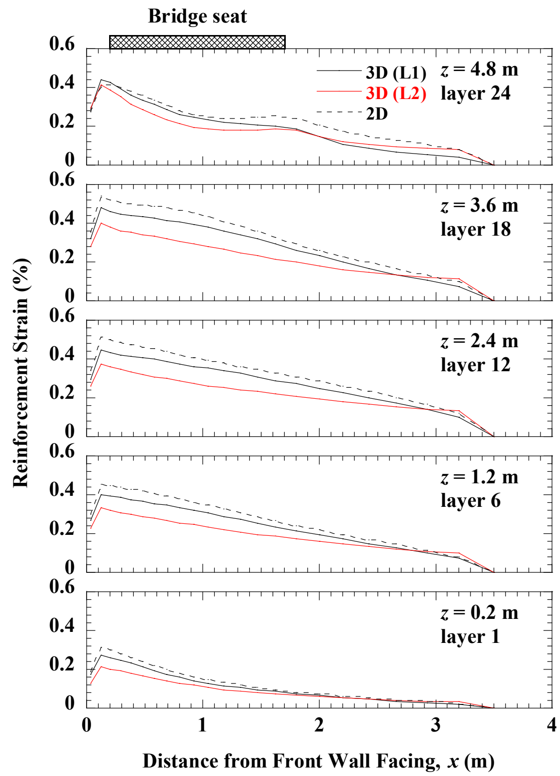

Figure 7 Reinforcement tensile strain distributions under q_v = 200 kPa

Reinforcement tensile strains for sections L1 and T1 under different levels of applied vertical stress are shown in Figure 8. As shown in Figure 8(a), tensile strains for section L1 increase significantly with increasing vertical stress, and the effect is more pronounced in the upper reinforcement layers. For $q_v \geqslant$ 200 kPa, the tensile strains in layer 24 under the heel of the bridge seat show a clear increase. As indicated in Figure 8(b), tensile strains for section T1 have maximum values under both edges of the bridge seat and decrease toward the center. Reinforcement strains are also significantly influenced by applied vertical stress in section T1, especially for the upper layers under the edges of the bridge seat. In general, the reinforcement tensile strains are strongly affected by applied vertical stress, and the maximum strains occur near the facing connections for section L1 and under both edges of the bridge seat for section T1, respectively.

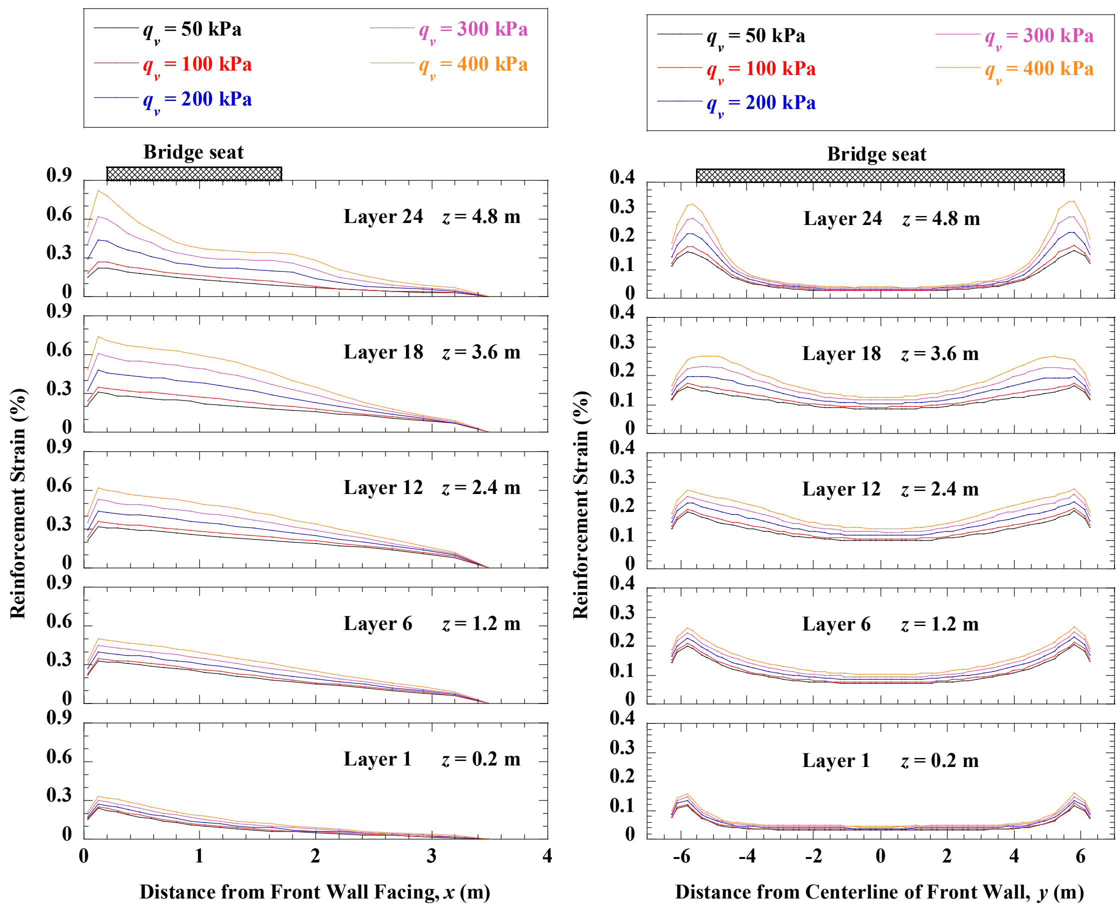

(a) (b)

Figure 8 Reinforcement tensile strain distributions: (a) longitudinal section L1; (b) transverse section T1

3.4 Reinforcement tensile forces

Vertical profiles of maximum tensile force for q_v = 200 kPa are presented in Figure 9(a). Profiles for longitudinal sections L1 and L2 show similar trends, with the maximum tensile force increasing gradually from the bottom to the top reinforcement layers. Maximum tensile forces for section L1 are generally 1 kN/m greater than those for section L2, with the highest values of 4.9 kN/m and 4.3 kN/m, respectively. Maximum tensile forces for section T1 are smaller than those for the longitudinal sections and are approximately 2 kN/m. Results from the 2D simulation are also provided in Figure 9(a) for comparison. The maximum tensile forces for the 2D simulation have essentially the same trend as for section L1 but with slightly larger values. The highest value for the 2D profile is 5.5 kN/m, located at z = 3.8 m.

The maximum tensile forces calculated using the stiffness method and the simplified method (AASHTO, 2020) for q_v = 200 kPa provided in Figure 9(a) for comparison. The incremental vertical stresses given by these methods are determined using a truncated 2:1 distribution. Calculated tensile forces given by the stiffness method increase from 3.6 kN/m at the bottom layer to 5.5 kN/m at z = 4.6 m, and then sharply increase to 6.7 kN/m at the top layer. Calculated values using the simplified method first decrease from the top with decreasing elevation till z = 4.0 m and then remain nearly constant toward the bottom. The discrepancies in calculated tensile forces for these two methods generally decrease with increasing elevation, and are similar in the upper layers ($z \geqslant$ 3.8 m). Both methods show good agreement with the simulated maximum tensile forces of section L1 at mid-height but are larger than the simulated values near the bottom and the top, with the stiffness method showing better agreement than the simplified method near the bottom for q_v = 200 kPa.

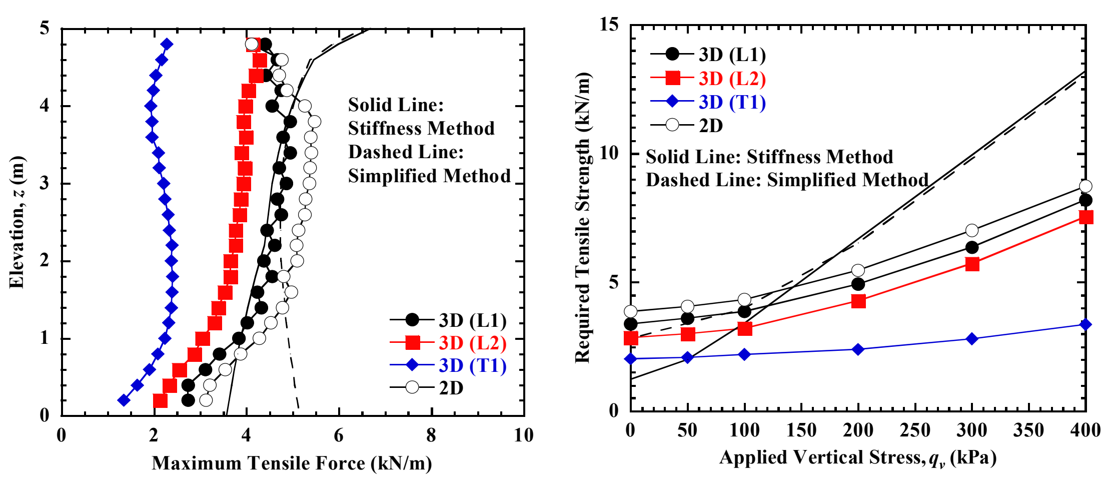

(a) (b)

Figure 9 Reinforcement tensile forces: (a) maximum tensile force profiles under q_v = 200 kPa; (b) required tensile strength

Figure 9(b) shows the variation of (factored) required tensile strength with vertical stress for the 2D and 3D simulations, where the required tensile strength is defined as the highest value for each maximum tensile force profile and represents factored values considering the reduction factors for installation damage, creep, and degradation. For the 3D simulations, the required tensile strengths for sections L1 and L2 show the same nonlinear increasing trend with increasing vertical stress, while the simulated values for T1 increase more slowly with vertical stress for the conditions investigated, especially at low stress conditions. The required tensile strengths for section L1 are consistently larger than those for other two sections (L2 and T1) with increasing vertical stress. For example, the required tensile strengths are 5.0 kN/m, 4.3 kN/m, and 2.4 kN/m for section L1, L2, and T1, respectively, under q_v = 200 kPa. The results confirm that the longitudinal centerline section for 3D conditions is the most critical (i.e., highest tensile stresses) for internal stability design. The required tensile strengths from the 2D simulations show the same trend as the longitudinal sections of the 3D simulations but are approximately 10% larger than those from the 3D simulations under the same applied vertical stress. This again demonstrates that the 2D simulation is more conservative than the 3D simulation.

Required reinforcement tensile strengths calculated using the stiffness method and the simplified method are also provided in Figure 9(b) for comparison. The simplified method shows larger required tensile strengths than the stiffness method for low vertical stresses, while the calculated values using the two methods are nearly the same for $q_v \geqslant 200$ kPa. In general, tensile strengths calculated using the simplified method are in reasonable agreement with the simulated values for section L1 for $q_v \leqslant 150$ kPa, while the stiffness method gives lower values, especially for low vertical stresses. Both methods overestimate the required tensile strengths for $q_v \geqslant 150$ kPa, and the deviations increase significantly with increasing vertical stress, which indicates that the both methods are overconservative for high vertical stresses.

4. Parametric study

A parametric study was conducted using the same 3D modeling approach to investigate the influences of abutment width and height on the 3D response of GRS bridge abutments for varying levels of applied vertical stress on the bridge seat. The baseline case corresponds to a beam width of w = 10 m and a lower GRS wall height of h = 5.0 m and other parameters as provided in the previous section. To investigate the influence of abutment width, values of beam width w = 10 m, 18 m, and 26 m are considered, and the abutment width is determined by assuming a setback distance of 0.9 m between the bridge seat and side wall facing. The corresponding abutment widths are 13.2 m, 21.2 m, and 29.2 m, respectively. Numerical simulations were conducted for a lower GRS wall height of h = 3 m, 5 m, and 7 m to evaluate the influence of abutment height. The height of upper GRS wall is held constant at 1.4 m. Therefore, the corresponding total abutment heights are 4.4 m, 6.4 m, and 8.4 m, respectively. In the parametric study, only the variable of interest in each series is changed, and the other parameters remain the same as those in the baseline case. Results are presented for facing displacements, settlements, and reinforcement tensile forces to evaluate the 3D response.

4.1 Influence of abutment width

4.1.1 Facing displacements

Facing displacement profiles for sections L1 and T1 under q_v = 200 kPa are shown in Figure 10(a). For section L1, facing displacements generally increase with increasing abutment width; however, the effect becomes less pronounced for wider abutments. This is observed as facing displacements for w = 18 m and 26 m are nearly equal. Transverse section T1 shows the same trend with small displacements. Figure 10(b) presents maximum facing displacements for different vertical stress levels and indicates similar trends.

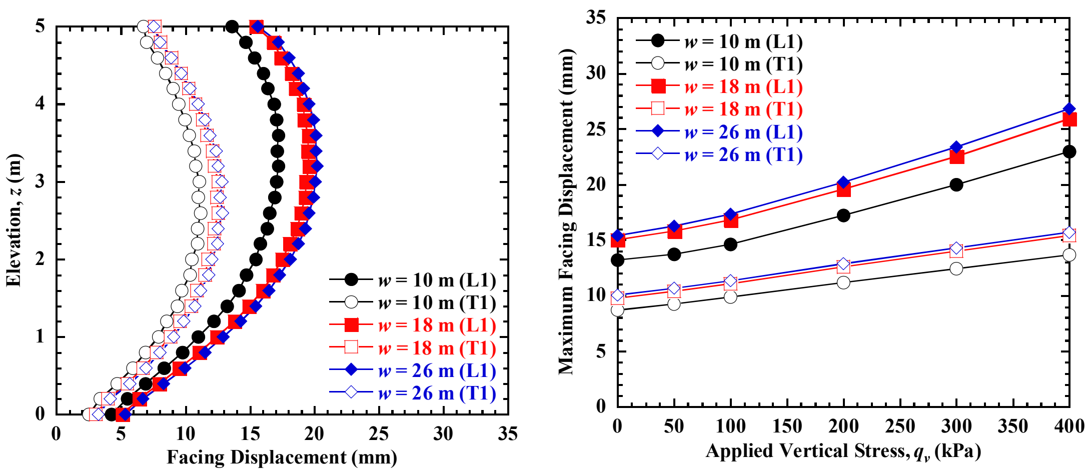

(a) (b)

Figure 10 Influence of abutment width on facing displacements: (a) vertical profiles under q_v = 200 kPa; (b) maximum displacements

Horizontal profiles of facing displacement for the front wall under q_v = 200 kPa and elevation z = 3.0 m are presented in Fig. 11(a). Distances from the centerline are normalized by abutment width. Similar to Fig. 10, facing displacements increase with abutment width but at a decreasing rate for wider abutments. Maximum displacements occur near the centerline of the front wall. The difference in facing displacements between the centerline and the edge of the front wall becomes larger for larger abutment width, which indicates that the 3D deformation response is more obvious for wider abutments. Figure 11(b) shows corresponding plots of facing displacement for the side wall (q_v = 200 kPa, z = 3.0 m). The influence of abutment width on these displacements is less pronounced and consistent with trends in Fig. 11(a).

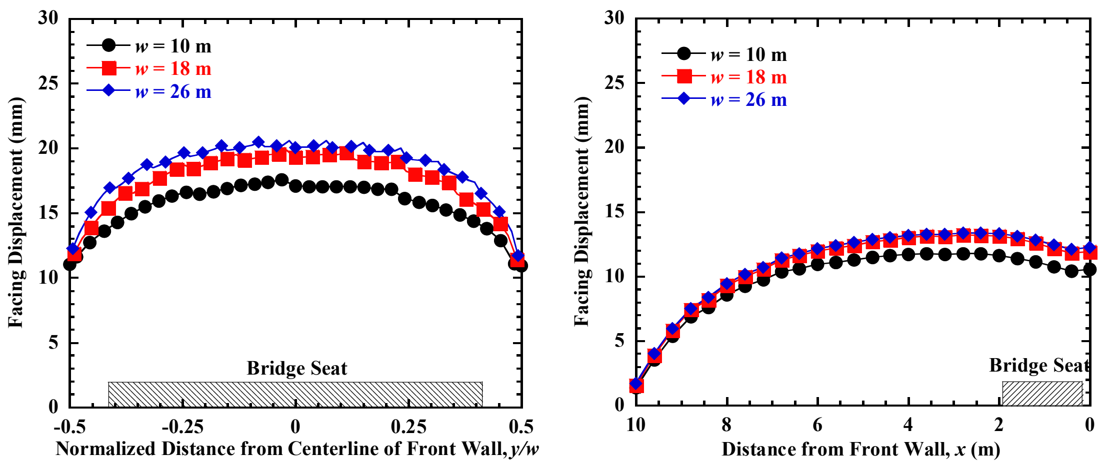

(a) (b)

Figure 11 Influence of abutment width on facing displacements under qv = 200 kPa and z = 3.0 m: (a) front wall; (b) side wall

Results in Figures 10 and 11 indicate that facing displacements generally increase with abutment width for 3D boundary conditions. For the front wall, as the abutment becomes wider, restraints provided by the two side walls decrease and, as a result, facing displacements at the longitudinal centerline section become increasingly larger. Facing displacements for the side walls increase with abutment width because the total applied load increases (i.e., a wider area is subjected to the bridge surcharge stress).

4.1.2 Bridge seat settlements

Figure 12 shows the influence of abutment width on bridge seat settlements. In general, the abutment width has little influence on settlements, especially for low vertical stress levels ($q_v \leqslant 200$ kPa). For higher vertical stresses, bridge seat settlements become increasingly larger for wider abutments, which is consistent with the larger facing displacements shown in Figure 10(b). In general, the influence of abutment width on bridge seat settlements is minimal for the service load conditions.

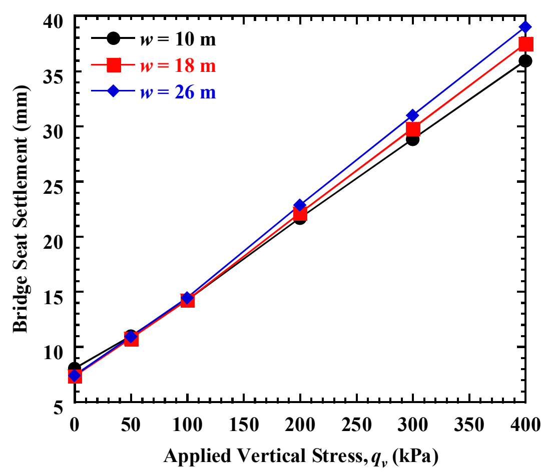

Figure 12 Influence of abutment width on bridge seat settlements

4.1.3 Reinforcement tensile forces

Figure 13(a) presents vertical profiles of maximum reinforcement tensile force under q_v = 200 kPa. All profiles show maximum tensile forces increasing rapidly from the bottom to approximately z = 1.5 m, then increasing slightly with the maximum at approximately z = 3.5 m, and finally decreasing slightly toward the top. Maximum tensile forces generally increase slightly with increasing abutment width, with the highest values of 5.0 kN/m, 5.2 kN/m, and 5.3 kN/m for w = 10 m, 18 m, and 26 m, respectively. The calculated maximum tensile forces using the stiffness method and the simplified methods are also shown for comparison. The calculated forces using the stiffness method generally increase with increasing elevation and show overestimations near top and underestimations for $z \leqslant 4.0$ m. The simplified method shows reasonable agreement with the simulated values at mid-height but overestimations toward the top and the bottom. Both methods are not in close agreement with the simulated results and predict highest forces at the top, which are greater than those from the simulations.

Figure 13(b) shows the required tensile strengths with increasing vertical stress. Results indicate that strengths increase slightly with increasing abutment width. Both the stiffness method and the simplified method show overestimations of required tensile strength for $q_v \geqslant$ 150 kPa, with the difference becoming increasingly larger for higher vertical stress levels. For $q_v \leqslant$ 150 kPa, the stiffness method significantly underestimates the required tensile strength, while the simplified method shows better agreement with the simulated values.

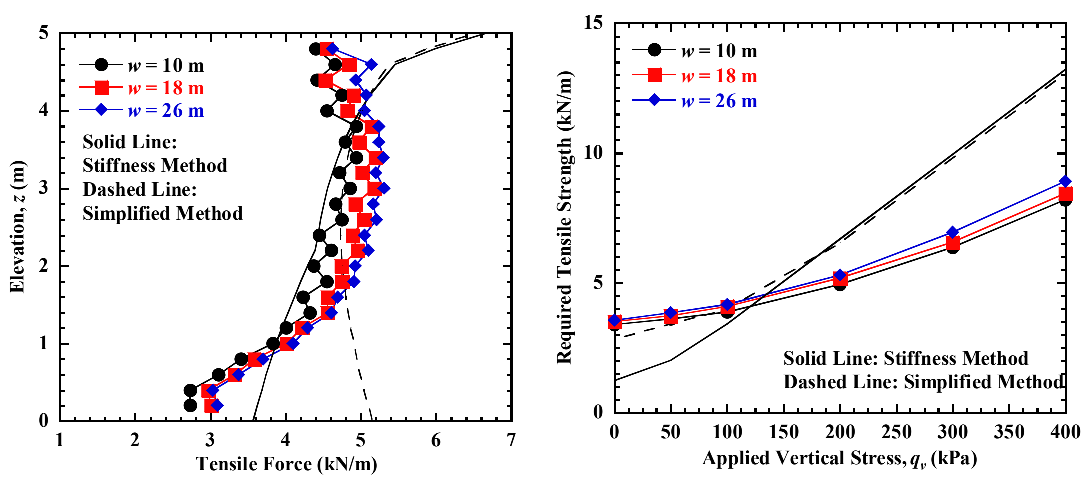

(a) (b)

Figure 13 Influence of abutment width on maximum tensile forces: (a) vertical profiles under q_v = 200 kPa; (b) required tensile strength

4.2 Influence of abutment height

4.2.1 Facing displacements

Vertical profiles of facing displacements, plotted versus normalized abutment height (z/h), and the corresponding maximum displacement of each profile for abutment height h = 3 m, 5 m, and 7 m are shown in Figure 14. In Figure 14(a), facing displacements increase significantly with increasing abutment height for both sections L1 and T1 under q_v = 200 kPa. In Figure 14(b), maximum values generally increase in a linear manner with increasing vertical stress for both sections for the range of stress conditions investigated, and the rate of increase for L1 is greater than for T1. Maximum displacements also increase with increasing abutment height for both sections. Interestingly, the increasing rates with increasing vertical stress are nearly the same for different abutment heights (i.e., the curves are parallel), which indicates that the influence on maximum displacements mainly comes from the construction of GRS abutments before placement of bridge beam.

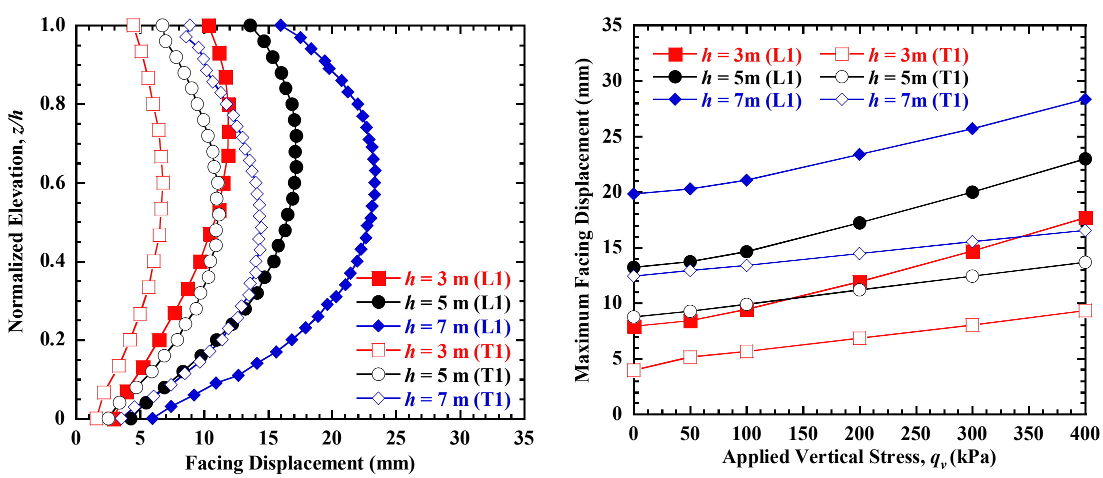

(a) (b)

Figure 14 Influence of abutment height on facing displacements: (a) vertical profiles under q_v = 200 kPa; (b) maximum displacements

The influence of abutment height on horizontal displacement profiles for the front and side walls at the normalized elevation z/h = 0.6 are shown in Figure 15. Figure 15(a) shows that facing displacement profiles of the front wall are similar for different abutment heights with obvious bulging deformations toward the longitudinal centerline and smaller displacements toward the side walls. Figure 15 indicates that facing displacements of the front wall and side wall are larger for taller abutments.

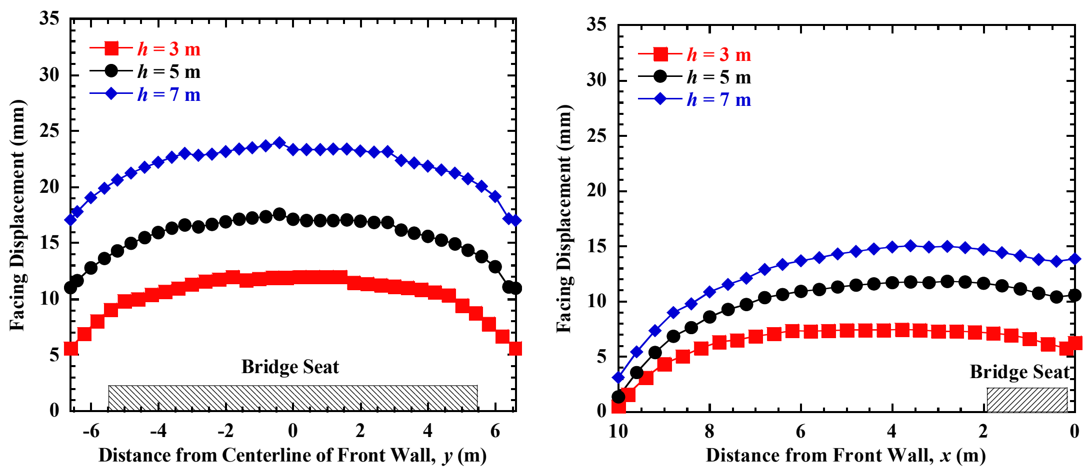

(a) (b)

Figure 15 Influence of abutment height on facing displacements at the normalized elevation z/h = 0.6: (a) front wall; (b) side wall

4.2.2 Bridge seat settlements

Figure 16(a) shows that bridge seat settlements increase nearly linearly with increasing vertical stress for different abutment heights. Taller abutments have larger bridge seat settlements, and the influence of abutment height is more pronounced for higher vertical stress levels. The corresponding abutment compressions (i.e., incremental values) due to the placement of the bridge beam, defined as the difference between the bridge seat settlement and foundation soil settlement, are shown in Figure 16(b). Results again indicate that the incremental settlements increase with abutment height; however, the influence becomes smaller for taller abutments, especially under high vertical stresses. For example, the incremental settlements for q_v = 200 kPa are 16.0 mm, 21.8 mm, and 25.5 mm for h = 3 m, 5 m, and 7 m, respectively, which correspond to compressional vertical strains of 0.31%, 0.25%, and 0.19%. Although taller abutments have larger bridge seat settlements and abutment compressions, the vertical strains decrease with increasing abutment height. This is attributed to the higher soil stiffness of backfill soil under larger stress conditions for taller abutments.

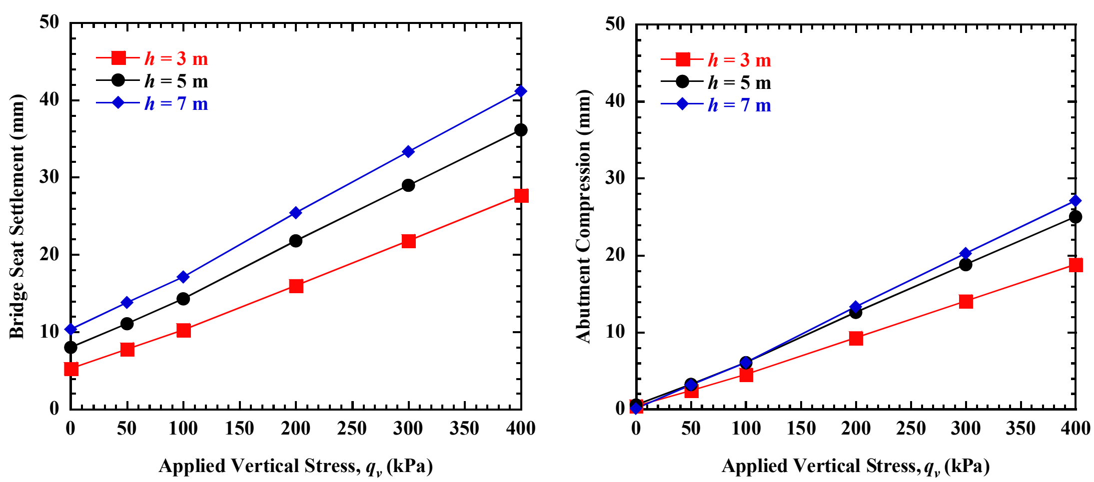

(a) (b)

Figure 16 Influence of abutment height on settlements: (a) bridge seat settlements; (b) abutment compression due to placement of bridge beam

4.2.3 Reinforcement tensile forces

Figure 17 shows maximum tensile force profiles and required tensile strengths for abutments with different abutment heights. As shown in Figure 17(a), maximum tensile forces generally increase with increasing abutment height due to the higher overall stress conditions. Calculated forces using the stiffness method and the simplified method are also provided for comparison. Both methods overestimate the maximum forces for h = 3 m and show reasonable estimations near the mid-height for h = 5 m but overestimations near the top and the bottom. For h = 7 m, both methods significantly underestimate the maximum forces at mid-height but show overestimations near the top and the bottom, with larger discrepancies observed for the stiffness method.

Figure 17(b) indicates that the required tensile strengths increase with increasing abutment height. Calculated values using the stiffness method show underestimations for low stresses and overestimations for high stresses. The simplified method also shows overestimations for high stresses but better agreement with the simulated values for low stresses, especially for h = 5 m and 7 m.

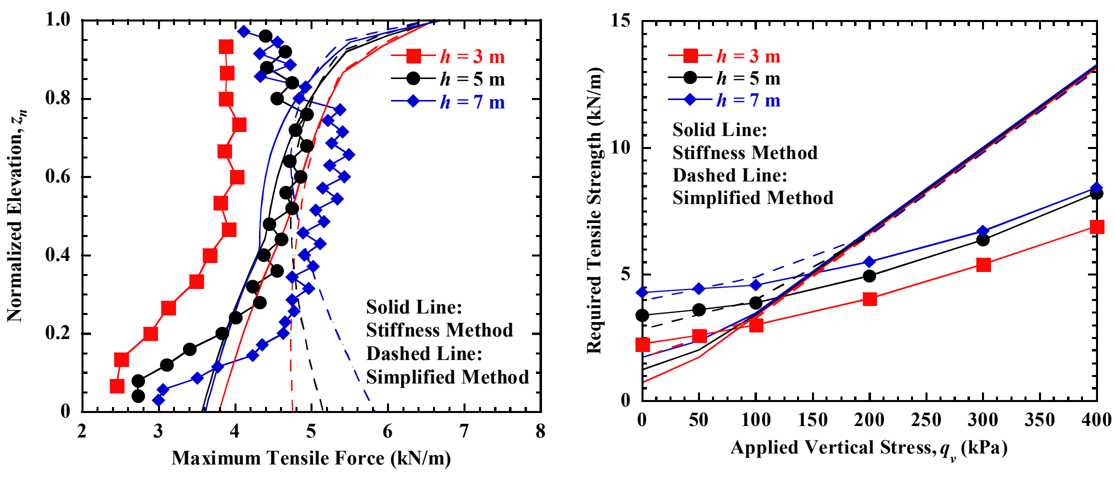

(a) (b)

Figure 17 Influence of abutment height on reinforcement tensile forces: (a) vertical profiles under q_v = 200 kPa; (b) required tensile strength

5. Conclusions

This paper presents numerical simulations of 3D deformation behavior of GRS bridge abutments for different geometry and loading conditions and results from corresponding 2D (plane strain) simulations. The following conclusions are reached for the conditions investigated:

(1) The application of bridge load produces lateral deformations of the abutment in different directions, showing typical 3D deformation behavior. Facing displacements for the longitudinal sections are larger than those for the transverse section. Facing displacements of the front wall and side walls generally increase with increasing abutment width, but the effect becomes less pronounced for wider abutments.

(2) Bridge seat settlement increases with increasing applied vertical stress in an approximately linear manner for service load conditions. Abutment width has little influence on bridge seat settlements, especially for low vertical applied stresses. Increasing abutment height leads to larger facing displacements, bridge seat settlements, and reinforcement tensile forces due to higher overall stress levels; however, the corresponding vertical strain decreases as the backfill soil becomes stiffer under greater stress levels.

(3) Maximum reinforcement tensile strains for the longitudinal and transverse sections occur near facing connections and under both edges of the bridge seat, respectively. Maximum

tensile forces of the longitudinal sections are larger than the transverse section, which indicates that the longitudinal section is more critical for the internal stability design.

(4) Both the stiffness method and the simplified method give overestimations of required reinforcement tensile strength for applied vertical stress greater than 150 kPa, and the difference becomes increasingly larger for higher levels of vertical applied stress. For applied vertical stress smaller than 150 kPa, the stiffness method significantly underestimates the required tensile strength, while the simplified method shows better agreement with the simulated values.

Declaration of competing interest

The authors declare that they have no known competing financial interests or personal relationships that could have appeared to influence the work reported in this paper.

Acknowledgments

This research is supported by the National Natural Science Foundation of China (Grant No. 52078392 and No. 52478358) and the National Key R&D Program of China (Grant No. 2022YFC3080400). The financial supports are greatly appreciated.

Notation

Basic SI units are given in parentheses.

B	bulk modulus (Pa)
c'	apparent cohesion (Pa)

c_i'	interface adhesion (Pa)
E	elastic modulus (Pa)
E_r	elastic modulus for reinforcement (Pa)
E_t	tangent elastic modulus (Pa)
E_{ur}	unloading–reloading modulus (Pa)
J	reinforcement secant stiffness
K	elastic modulus number (dimensionless)
K_b	bulk modulus number (dimensionless)
K_{ur}	unloading–reloading modulus number(dimensionless)
m	bulk modulus exponent (dimensionless)
n	elastic modulus exponent (dimensionless)
p_a	atmospheric pressure (Pa)
q_v	applied vertical stress on lower GRS wall (Pa)
RF_i	reduction factor for soil interface shear strength(dimensionless)
R_f	failure ratio (dimensionless)
tr	thickness of reinforcement (m)
x	distance from front wall facing (m)
y	distance from west side wall facing (m)
z	elevation above foundation soil (m)
γ	soil unit weight (N/m^3)
γ_b	equivalent unit weight of bridge beam (N/m^3)
δ_i'	interface friction angle (°)
v	Poisson's ratio (dimensionless)
v_t	tangent Poisson's ratio (dimensionless)
σ_1'	major principal effective stress (Pa)
σ_3'	major principal effective stress (Pa)
ϕ'	friction angle (°)

Abbreviations

2D	two-dimensional
3D	three-dimensional
AASHTO	American Association of State Highway and Transportation Officials
GRS	geosynthetic reinforced soil

References

Abu-Hejleh, N., Zornberg, J.G., Wang, T. and Watcharamonthein, J., 2002. Monitored Displacements of Unique Geosynthetic-Reinforced Soil Bridge Abutments. Geosynthetics International, 9(1), 71-95.

Abu-Farsakh, M., Ardah A., Voyiadjis, G., 2018. 3D Finite element analysis of the geosynthetic reinforced soil-integrated bridge system (GRS-IBS) under different loading conditions. Transportation Geotechnics, 15, 70-83.

Ambauen, S., Leshchinsky, B., Xie, Y. and Rayamajhi, D., 2016. Service-state behavior of reinforced soil walls supporting spread footings: a parametric study using finite-element analysis. Geosynthetics International, 23(3), 156-170.

Ardah, A., Abu-Farsakh, M. and Voyiadjis, G., 2017. Numerical evaluation of the performance of a Geosynthetic Reinforced Soil-Integrated Bridge System (GRS-IBS) under different loading conditions. Geotextiles and Geomembranes, 45(6), 558-569.

Ardah, A., Abu-Farsakh M., Voyiadjis, G., 2021. Numerical parametric study of geosynthetic reinforced soil integrated bridge system (GRS-IBS). Geotextiles and Geomembranes, 49(1), 289-303.

Deng, J., Zhang, J., Qi, Z., Zheng, Y., Zheng, J.-j., 2023. Experimental study on the load bearing behavior of geosynthetic reinforced soil bridge abutments on yielding foundation. Geotextiles and Geomembranes.

Deng, J., Guo, W., Jiang, Y., Zheng, J. J., Zheng, Y., 2025. Influence of foundation soil conditions on the service performance of GRS abutments. Geosynthetics International.

Gebremariam, F., Tanyu, B. F., Christopher, B., Leshchinsky, D., Han, J. and Zornberg, J. G., 2020. Evaluation of vertical stress distribution in field monitored GRS-IBS structure. Geosynthetics International, 27(4), 414–431.

Gebremariam, F., Tanyu, B. F., Christopher, B., Leshchinsky, D., Zornberg, J. G. and Han, J., 2020. Evaluation of required connection load in GRS-IBS structures under service loads. Geosynthetics International, 27(6), 620–634.

Gebremariam, F., Tanyu, B. F., Güler, E., Urgessa, G. S. and Shen, P., 2021. Numerical investigation of reinforced soil structures with GRS-IBS design features. Geosynthetics International, 28(1), 95–112.

Gebrenegus, T., Nicks, J., and Adams, M. (2015). "Large diameter triaxial testing of AASHTO open graded aggregates and the effect of relative density on strength." IFCEE 2015, ASCE, Reston, VA, 1870–1879.

Hatami, K. and Bathurst, R. J. (2006). Numerical model for reinforced soil segmental walls under surcharge loading. Journal of Geotechnical and Geoenvironmental Engineering, 132(6), 673–684.

Helwany, S. M. B., Wu, J. T. H. and Froessl, B., 2003. GRS Bridge abutments – an effective means to alleviate bridge approach settlement. Geotextiles and Geomembranes, 21(3), 177–196.

Helwany, S.M.B., Wu, J.T.H. and Kitsabunnarat A., 2007. Simulating the Behavior of GRS Bridge Abutments. Journal of Geotechnical and Geoenvironmental Engineering, 133(10), 1229-1240.

Iwamoto, M.K., Ooi, P.S.K., Adams, M.T. and Nicks, J.E., 2015. Composite properties from instrumented load tests on mini-piers reinforced with geotextiles. Geotechnical Testing Journal, 38(4), 397 – 408.

Jia, Y., Zhang, J., Tong, L., Zheng, J. J., Zheng, Y., 2025. Cumulative deformation behavior of GRS bridge abutments under cyclic traffic loading. Geosynthetics International, 32(1), 94-108.

Jia, Y., Wu, Q., Zhang, J., Zheng, Y., 2025. Load transfer and failure mechanisms of GRS bridge abutments: Insights from DEM simulations. Computers and Geotechnics, 180, 107088.

Michael T. Adams, Phillip S. K. Ooi and Jennifer E. Nicks.,2014, Mini-pier testing to estimate performance of full-scale geosynthetic reinforced soil bridge abutments. Geotechnical Testing Journal, 37(5), 1-11.

Nicks, J. E., Esmaili, D. and Adams, M. T., 2016. Deformations of geosynthetic reinforced soil under bridge service loads. Geotextiles and Geomembranes, 44(4), 641–653.

Pham, T. Q., 2009. Investigating Composite Behavior of Geosynthetic Reinforced Soil (GRS) Mass. PhD thesis, University of Colorado, Denver, USA.

Rong, W., Zheng, Y., McCartney, J. S. & Fox, P. J. (2017). 3D Deformation behavior of geosynthetic reinforced soil bridge abutments. Geotechnical Frontiers 2017, Florida, USA, March 2017, ASCE, Reston, VA, USA, pp. 44–53.

Saghebfar, M., Abu-Farsakh M., Ardah A., Chen Q., Fernandez B.A., 2017. Performance monitoring of Geosynthetic Reinforced Soil Integrated Bridge System (GRS-IBS) in Louisiana. Geotextiles and Geomembranes, 45(2), 34-47.

Skinner, G.D., Rowe, R. K., 2005. Design and behaviour of a geosynthetic reinforced retaining wall and bridge abutment on a yielding foundation. Geotextiles and Geomembranes, 23(3), 234–260.

Shen, P., Han, J., Zornberg, J.G., Tanyu B.F., Christopher B.R., Leshchinsky, D., 2020. Responses of geosynthetic-reinforced soil (GRS) abutments under bridge slab loading: Numerical investigation. Computers and Geotechnics, 123, 103566.

Shen, P., Han, J., Zornberg, J.G., Morsy, A.M., Leshchinsky, D., Tanyu, B.F., Xu, C., 2019. Two and three-dimensional numerical analyses of geosynthetic-reinforced soil (GRS) piers. Geotextiles and Geomembranes, 47(3), 352-368.

Soderman, K.L., and Giroud, J.P. (1995). Relationships between uniaxial and biaxial stresses and strains in geosynthetics. Geosynthetics International, 2(2), 495-504.

Talebi M., Meehan C.L., Leshchinsky D., 2017. Applied bearing pressure beneath a reinforced soil foundation used in a geosynthetic reinforced soil integrated bridge system. Geotextiles and Geomembranes, 45(6), 580-591.

Verma, A., Mittal, S., 2023. Comparative assessment of stability of GRS abutments through 1 g physical model tests for field implementation. Transportation Geotechnics, 42, 101056.

Wang, Q., Xu, C., Li, G., Shen, P., Zhao, C., 2025. Centrifuge modeling on the geosynthetic-reinforced soil (GRS) abutments with different combinations of reinforcement spacing and tensile stiffness. Geotextiles and Geomembranes, 53(6), 1473-1482.

Wu, J. T. H., Ketchart, K. & Adams, M., 2001. GRS Bridge Piers and Abutments, Report No. FHWA-RD-00-038. US DOT, Washington, DC, USA.

Xiao, C., Han, J. and Zhang, Z., 2016. Experimental study on performance of geosynthetic-reinforced soil model walls on rigid foundations subjected to static footing loading. Geotextiles and Geomembranes, 44(1), 81–94.

Xu, C., Liang, C. and Shen, P., 2019. Experimental and theoretical studies on the ultimate bearing capacity of geogrid-reinforced sand. Geotextiles and Geomembranes, 47(3), 417–428.

Xie, Y. and Leshchinsky, B., 2015. MSE walls as bridge abutments: Optimal reinforcement density. Geotextiles and Geomembranes, 43(2), 128-138.

Zhang, J., Guo, W., Ji, M., Zhao, J., Xu, C. and Zheng, Y., 2022. Field monitoring of vertical stress distribution in GRS-IBS with full-height rigid facings. Geosynthetics International, 29(6), 610-621.

Zheng, Y. and Fox, P.J., 2016. Numerical Investigation of Geosynthetic-Reinforced Soil Bridge Abutments under Static Loading. Journal of Geotechnical and Geoenvironmental Engineering, 142(5), 04016004.

Zheng, Y. and Fox, P.J., 2017. Numerical Investigation of the Geosynthetic Reinforced Soil–Integrated Bridge System under Static Loading. Journal of Geotechnical and Geoenvironmental Engineering, 143(6), 04017008.

Zheng, Y., Fox, P. J. and McCartney, J. S., 2018a. Numerical simulation of the deformation response of geosynthetic reinforced soil mini-piers. Geosynthetics International, 25(3), 271-286.

Zheng, Y., Fox, P.J., McCartney, J.S., 2018b. Numerical simulation of deformation and failure behavior of geosynthetic reinforced soil bridge abutments. Journal of Geotechnical and Geoenvironmental Engineering. 144(7), 04018037.

Zheng, Y., Fox, P. J., Shing, P. B. & McCartney, J. S. (2019a). Physical model tests of half-scale geosynthetic reinforced soil bridge abutments. I: Static loading. Journal of Geotechnical and Geoenvironmental Engineering, 145(11), 04019094.

Zheng, Y., Guo, W., Fox, P. J. and McCartney, J. S. (2021). 2D and 3D simulations of static response of a geosynthetic reinforced soil bridge abutment. Geosynthetics International, 29(5), 534-546.